JOM, Vol. 70, No. 4, 2018
https://doi.org/10.1007/s11837-017-2714-y
© 2018 The Minerals, Metals & Materials Society

Structural Evolution of Q-Carbon and Nanodiamonds

SIDDHARTH GUPTA,[1] ANAGH BHAUMIK,[1] RITESH SACHAN,[1,2] and JAGDISH NARAYAN[1,3]

1.—Department of Materials Science and Engineering, Centennial Campus, North Carolina State University, Raleigh, NC 27695-7907, USA. 2.—Materials Science Division, Army Research Office, Research Triangle Park, NC 27709, USA. 3.—e-mail: narayan@ncsu.edu

This article provides insights pertaining to the first-order phase transformation involved in the growth of densely packed Q-carbon and nanodiamonds by nanosecond laser melting and quenching of diamond-like carbon (DLC) thin films. DLC films with different sp^3 content were melted rapidly in a controlled way in super-undercooled state and quenched, leading to formation of distinct nanostructures, i.e., nanodiamonds, Q-carbon, and Q-carbon nanocomposites. This analysis provides direct evidence of the dependence of the super-undercooling on the structural evolution of Q-carbon. Finite element heat flow calculations showed that the super-undercooling varies monotonically with the sp^3 content. The phenomenon of solid–liquid interfacial instability during directional solidification from the melt state is studied in detail. The resulting lateral segregation leads to formation of cellular filamentary Q-carbon nanostructures. The dependence of the cell size and wavelength at the onset of instability on the sp^3 content of DLC thin films was modeled based on perturbation theory.

INTRODUCTION

The first successful experimental demonstration of conversion of carbon to diamond and Q-carbon was achieved by Narayan et al.[1,2] based on irradiation of carbon films with nanosecond laser pulses. Formation of Q-carbon and diamond by nanosecond laser melting of amorphous carbon thin films has motivated profound interest in the thermodynamics and kinetics that underpin such nonequilibrium phase transformations.[2] Ultrafast quenching with super-undercooling drives formation of Q-carbon ($\sim$ 80% sp^3 content) from the melt state.[2–4] We have also grown nanoneedles, microneedles of diamond, and epitaxial diamond thin films on sapphire.[3] Upon further increase in undercooling, conformal coatings of Q-carbon nanocomposite form on r-sapphire substrates, exhibiting superior mechanical properties such as hardness, wear resistance, adhesion to the substrate, and friction coefficient in comparison with industrial-grade DLC coatings.[4] We demonstrated that sp^2 dangling bonds inside the Q-carbon matrix generate robust room-temperature ferromagnetism in Q-carbon.[2,4] As Q-carbon forms via nonequilibrium processing, it is possible to introduce dopants above retrograde thermodynamic solubility limits by solute trapping simultaneously with melt quenching. This phenomenon has enabled incorporation of up to 50% boron in Q-carbon which is significantly above the solubility limit, leading to Bardeen–Cooper–Schrieffer (BCS) superconductivity temperature (T_c) of 56 K and higher.[5] We also doped Q-carbon with nitrogen, leading to formation of pristine nitrogen vacancy (NV) centers upon further processing, for use in quantum computing applications.[6] These breakthroughs led to modifications in the carbon phase diagram, as diamond can now be fabricated in ambient conditions. Due to the interest in such novel properties exhibited by pristine and doped Q-carbon and their derivatives, a detailed account pertaining to the thermodynamic considerations regarding the structural evolution of Q-carbon from melt state is presented herein. This growth model is based on previous analysis of melting and homogeneous crystal regrowth in other tetrahedrally bonded single-element systems such as silicon.[7]

EXPERIMENTAL PROCEDURES

Diamond-like carbon (DLC) films were deposited on r-sapphire substrate by laser ablation of a glassy carbon target, using a krypton fluoride excimer laser with full-width at half-maximum (FWHM) of

(Published online January 3, 2018)

25 ns, wavelength of 248 nm, and energy density of ~ 3.0 J cm^{-2}, to thickness of ~ 500 nm under high vacuum of 1×10^{-6} Torr inside the pulsed laser deposition (PLD) chamber at room temperature. Variation of the target ablation spot size was used to control the sp^3 content in the as-deposited film. The sp^3 content in the DLC thin film increases on creating a forward-directed laser plume. Using a point-source plume, one can achieve $\sim 10\%$ sp^3, while on rendering the plume more forward directed, the sp^3 content in the DLC film rises to $\sim 90\%$. Subsequently, pulsed laser annealing (PLA) was performed on the films using 193-nm 20-ns argon fluoride excimer laser pulses with energy density of 0.8 J/cm^2. A WITec confocal Raman microscope system (Alpha 3000 M, 532 nm source) was utilized to characterize the Raman-active vibrational modes in as-deposited and laser-annealed samples. The Raman acquisitions were calibrated using single-crystal Si with a characteristic Raman peak at 520.6 cm^{-1}. High-resolution scanning electron microscopy (SEM) images were acquired in backscattering mode for structural analysis and phase identification using an FEI Verios 460L field-emission scanning electron microscope (FESEM). A JEOL2010F was used to perform high-resolution transmission electron microscopy (HRTEM) imaging and electron energy loss spectroscopy (EELS) analysis.

RESULTS AND DISCUSSION

When carbon melts on a thermally insulating substrate, quenching occurs from the super-undercooled state. Upon laser irradiation, DLC melts and forms liquid carbon, which is metallic. The liquid carbon undergoes super-undercooling at the substrate–liquid carbon interface, leading to formation of diamond or Q-carbon, depending on the extent of undercooling. It is worth mentioning that the sp^3-hybridized atomic orbitals mobilize with heat flux, resulting in formation of Q-carbon at the melt–substrate interface and thus reducing the overall sp^3 content in the melt overlayer. This leads to microstructural evolution of these structures towards the film overlayer.

Figure 1a and b shows Raman spectra of as-deposited DLC and Q-carbon nanostructures, respectively. A Voigt profile containing a convolution of Gaussian and Lorentzian profiles can be accurately fit to the acquired Raman spectra. The peak positions were fixed at 1140 cm^{-1} (T peak), 1332 cm^{-1} (D peak), and 1580 cm^{-1} (G peak), corresponding to Raman-active vibrational modes. The minimum sp^3 content in the DLC film which led to formation of Q-carbon nanostructures was determined to be 16%, as shown in Fig. 1a. Upon performing PLA, there was an abrupt change in the Raman acquisitions near the Q-carbon nanostructures, as shown in Fig. 1b. There was a noticeable rise in the T and D peak intensities for the Q-carbon nanostructures, corresponding to an increase in sp^3-sp^3 bonded nanoclusters and sp^3 hybridized atomic orbitals in the amorphous matrix, respectively. Here, the sp^3 content was determined to be $\sim 81\%$. The peak shoulder at ~ 1331 cm^{-1} corresponds to presence of nanodiamonds near Q-carbon nanostructures. Post-PLA, formation of localized Q-carbon nanostructures together with conformal coverage of nanodiamonds in the melted region is revealed in Fig. 1c. As the melt quenches, phase segregation of sp^2 and sp^3 atoms becomes energetically favorable, leading to transverse diffusion of sp^2 and sp^3 hybridized atomic orbitals. The ultrafast quenching arrests the sp^2 and sp^3 orbital diffusion and determines the resulting nanostructures. At low regrowth velocities, sp^3 and sp^2 orbitals have sufficient time to rearrange themselves, resulting in formation of thermodynamically stable crystalline phases. The Q-carbon nanostructure width is ~ 300 nm with nanodiamonds embedded in it (Fig. 1d). There are regions inside the Q-carbon filament where it has broken down, providing nucleation sites for diamond epitaxial regrowth from the melt state. The inset in Fig. 1d shows homogeneous nucleation of diamonds, leading to formation of clusters with size of ~ 10 nm.[2,3] To analyze the effect of DLC on Q-carbon formed after PLA, films with moderate sp^3 content of $\sim 50\%$ were grown, as shown in Fig. 2a. The 1332 cm^{-1} peak shoulder of diamond is absent from the Q-carbon spectra in Fig. 2b. The SEM image in Fig. 2c shows no evidence of nanodiamond nucleation. The high-resolution SEM backscattering image in Fig. 2d shows a single Q-carbon filamentary nanostructure with minimal porosity and width of ~ 250 nm.

The maximum sp^3 fraction in the DLC films resulting in Q-carbon formation and successful laser melting was determined to be $\sim 80\%$, as shown in Fig. 3a. As the thermal conductivity of 80% sp^3 DLC thin film is high, the whole laser-annealed region melts, leading to formation of Q-carbon nanostructures throughout the substrate. Figure 3c shows conformal coverage of Q-carbon cellular nanostructures on the sapphire substrate. Post-PLA, phase segregation occurs in the film, leading to formation of distinct Q-carbon and α-carbon phases; Fig. 3b shows their respective Raman spectra. The Q-carbon phase has 82% sp^3 content, consistent with previous reports, whereas the α-carbon phase has 40% sp^3 content. Phase segregation is evident in Fig. 3d, highlighting distinct α-carbon and Q-carbon phases. Moreover, no interdiffused region is observed between Q-carbon and α-carbon phases, due to the decreased miscibility of sp^3 in sp^2 hybridized orbitals upon quenching, as shown in Fig. 3d. The high-resolution image shows a single cell structure with cell size of ~ 2 μm, and wave-like regions arising from sp^3 solute segregation. We observe a sharp interface between the α- and Q-carbon phases, due to the ultrafast nature of the quenching and strong undercooling. The inherent

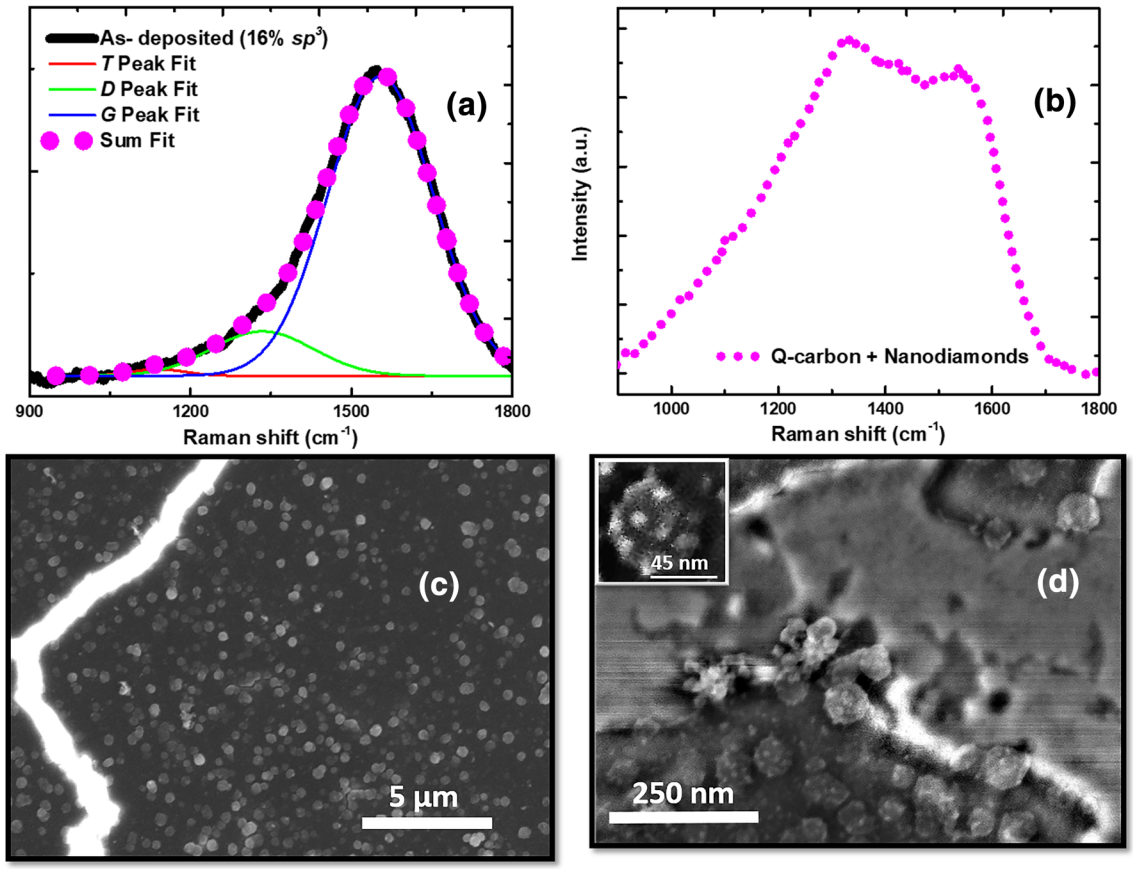

Fig. 1. Raman spectroscopy of (a) as-deposited DLC (~ 16% sp^3 content), (b) 1-shot laser annealed Q-carbon and nanodiamonds, (c) Low magnification SEM backscattering image showing nanodiamonds and a single Q-carbon filament, (d) high-resolution SEM backscattering image illustrating a singular Q-carbon filamentary nanostructure along with homogenous nanodiamond growth.

porosity of ~ 40 nm and randomness of these nanostructures highlight faster quenching and phase segregation compared with low- and medium-sp^3 as-deposited thin films.

Crystal growth from an amorphous matrix is associated with a first-order phase transformation; i.e., growth proceeds with motion of the interface between the two coexisting phases. PLA of DLC films leads to growth rates orders of magnitude higher than conventional crystal growth rates.[2] The nature of such growth is dependent on the incorporation rate of carbon atoms from the amorphous phase into the crystalline phase. In the case of silicon or gallium arsenide, upon increasing the regrowth velocity, increased numbers of defects and twins are introduced, while a further rise in regrowth rates leads to formation of amorphous matrix as final product.[7]

Upon increasing the sp^3 content in the as-deposited thin film, above a certain concentration, crystallization of nanodiamonds ceases to occur, with complete amorphization upon regrowth of the melt state. This transition is observed when the super-undercooling renders the rate of amorphization faster than that of crystallization. In nanosecond laser melting, the melt regrowth velocity is a peaked function of the undercooling, due to viscosity effects.[8] The net rate of atomic jumping for interfacial regrowth at a liquid–solid interface for nonequilibrium processing at temperature T is given by

$$V \sim \frac{D_\alpha f}{\lambda f_D}\left(1 - e^{\frac{-\Delta G_T}{kT}}\right), \quad (1)$$

where D_α is the diffusivity in the melt near the interface (~ 10^{-8} m^2 s^{-1}), f_D is the geometric factor associated with diffusion (= 1 for isotropic amorphous melt), f is the fraction of sites available for atomic exchange (= 1 for continuous growth from metallic melt), and is the atomic jump distance across the melt interface,[9] given as 1.31 Å for carbon.[10] As amorphization and crystallization both occur from the melt state, they compete kinetically during regrowth:

$$G_m = \Delta H - T_m \Delta S_m, \quad (2)$$

$$\Delta G_u = \Delta H - T_u \Delta S_u, \quad (3)$$

$$\Delta G_T = (\Delta G_m - \Delta G_u) = T_u \Delta S_u - T_m \Delta S_m, \quad (4)$$

where $\Delta T_u = T_u - T_m$ is the observed undercooling.

The subscripts "u" and "m" indicate the material in undercooled and melt state, respectively.

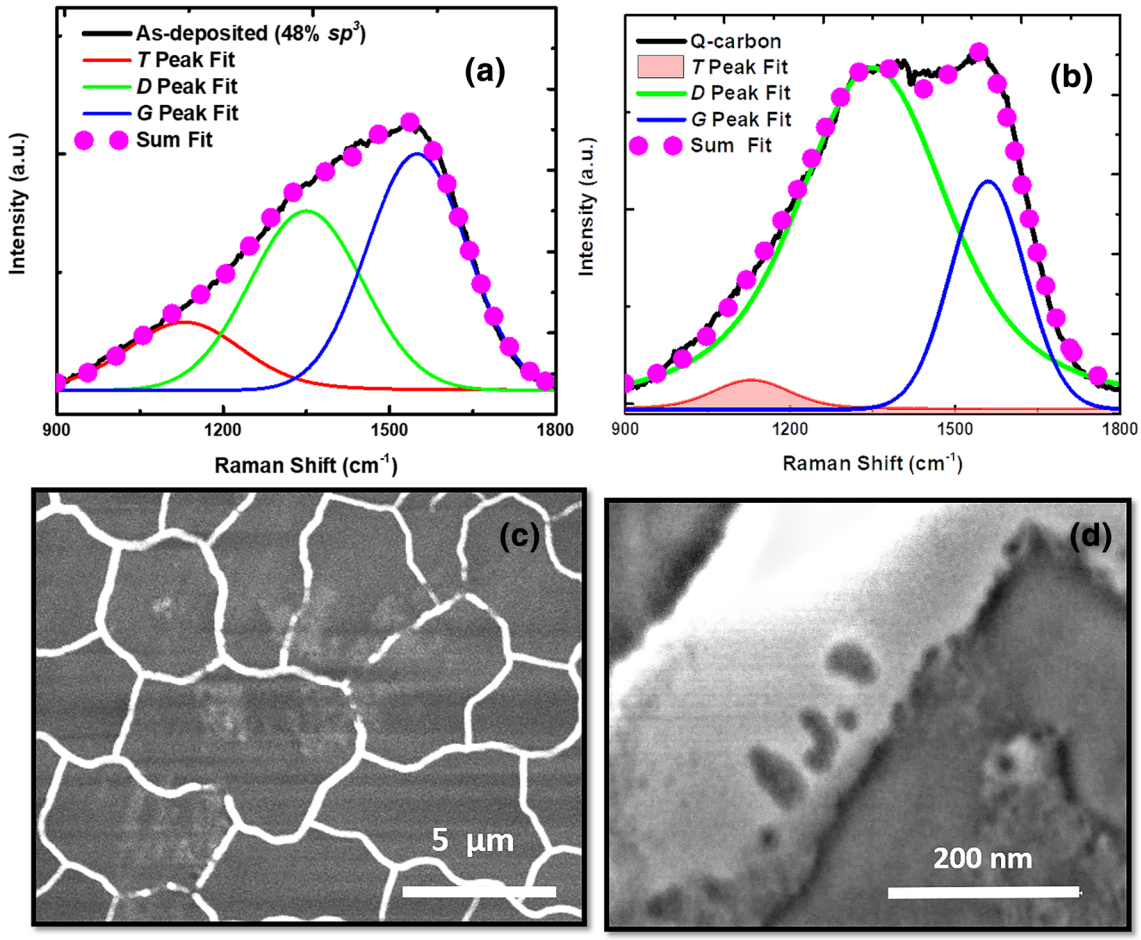

Fig. 2. Raman spectroscopy of (a) as-deposited DLC (~ 48% sp^3 content), (b) PLA-processed Q-carbon nanostructures, (c) SEM image showing Q-carbon filamentary nanostructures, (d) high-resolution SEM image illustrating a singular Q-carbon filamentary nanostructure with minimal porosity.

Here, the melting temperatures are $T_m^d \sim 5000$ K and $T_m^\alpha \sim 4000$ K, and the specific heat capacities are $C_p^\alpha = 5.833$ J/mol-K and $C_p^d = 2.448$ J/mol-K.[11] The superscripts "d" and "α" indicate diamond and amorphous solid state, respectively.

There is the thermodynamic possibility of amorphous regrowth at the solid–liquid interface above a critical undercooling (ΔT_c).[10]

$$\Delta T_c > T_m^d - T_m^a \quad (5)$$

In the case of carbon, $\Delta T_c \sim 1000$ K. Once the undercooling exceeds ΔT_c, the microstructure changes from nanodiamonds to amorphous Q-carbon. At low regrowth velocity of ~ 1–2 m s^{-1}, the undercooling is low and formation of graphite occurs. Upon rise in the regrowth velocity, the undercooling should increase, leading to growth of diamonds. PLA of DLC with 16% sp^3 content resulted in predominant growth of nanodiamonds. Above a critical regrowth velocity, amorphous regrowth becomes energetically favorable as compared with nanodiamond nucleation. At this point, formation of only amorphous Q-carbon should be observed. Solving Eq. 1 with ΔG_a instead of ΔG_d, we calculated ~ 16 m s^{-1} as the critical velocity above which complete amorphization of the melt occurs. In the intermediate range, due to the ultrafast quenching, it is possible to form twinned nanodiamonds and Q-carbon. In silicon, twinning is observed in the intermediate nanocrystal–amorphization range.[12]

In the case of temporally extended laser annealing, crystallites have sufficient time to nucleate at the ascending solid–liquid interface. Therefore, nuclei can grow homogeneously throughout the interface, releasing excess latent heat of fusion which can be utilized to further extend the melt spatially. This process ends when the latent heat produced is insufficient to melt the underlayer. For shorter pulses, regrowth velocities are higher, suppressing nanodiamond nucleation at the solid–liquid interface. The high thermal conductivity of liquid carbon causes a dip in the melt temperature below T_m^α. This leads to the onset of amorphous phase regrowth. To understand the mechanism behind the evolution of the Q-carbon nanostructures on laser annealing, we simulated the laser interactions utilizing extremely accurate heat flow equations on PLA-processed DLC by employing laser–solid melt interactions (SLIM).[13] The thermal

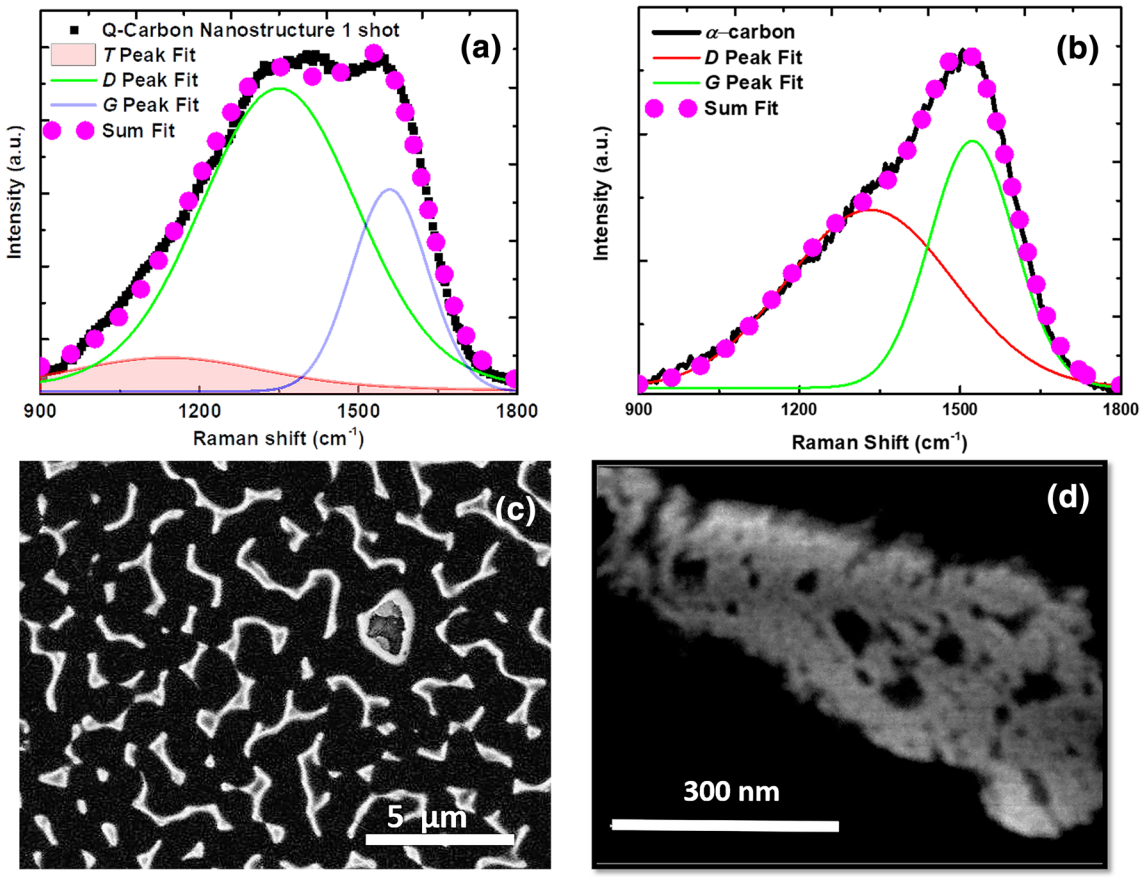

Fig. 3. Raman spectroscopy of 1-shot PLA processed (a) α-carbon, (b) Q-carbon nanostructures inside the nanocomposites formed from 80% sp^3 DLC, (c) SEM image showing the conformal coverage of Q-carbon embedded in α-carbon matrix, (d) high-resolution SEM image illustrating a singular Q-carbon filamentary nanostructure.

conductivity of DLC thin films increases monotonically with increasing sp^3 content.[14] Figure 4a depicts the temperature profiles corresponding to the surface of the thin films. Distinct phase transformations can be noted as the film changes from solid to liquid at 4000 K and back to solid by distinct cusps on the profile at 30 ns and 150 ns, respectively. The inset in Fig. 4a demonstrates heating of the liquid above 4000 K. This also provides an estimate of the ripples/onset of instability at the surfaces, as substantial thermal gradients are established when the surface begins to melt. It is evident from these curves that quenching from the melt front increases with increasing sp^3 content of the thin film.

The thermal profile for 10% sp^3 DLC film in Fig. 4a reveals that, post-PLA, the surface remains molten for more than 500 ns. Such low thermal gradients should cause low undercooling. It is reasonable to expect crystalline epitaxial regrowth in such conditions, as depicted in Fig. 1 for PLA-processed 16% sp^3 DLC film. Figure 4b depicts the structure and bonding analysis of single-crystal diamond formed after a rapid crystallization process from Q-carbon. HRTEM indicates presence of pristine diamond (post-PLA) with no evidence of graphitic entities. In the selected-area diffraction pattern, two sets of (111) and one set of (002) diffraction spots are observed, indicating growth of ⟨110⟩ diamond, consistent with the ⟨110⟩ silicon formed by rapid seeded crystallization.[15] The Q-carbon phase has ∼ 80% sp^3 (diamond nuclei), while the rest is sp^2. The sp^3 entities (nanodiamonds) facilitate growth of ⟨110⟩ diamond via homogeneous nucleation. For further investigation of the bonding characteristics, room-temperature core-loss EELS measurements were undertaken. The spectrum shows an evident characteristic σ^* peak (at ∼ 292 eV), corresponding to sp^3-bonded carbon. The sharpness of the σ^* peak also indicated long-range ordering in the diamond structure. The absence of the π^* peak (at ∼ 285 eV) indicates formation of diamond after the rapid crystallization process from Q-carbon. Therefore, our novel PLA technique coupled with theoretical calculations form the basis for creation of single-crystal diamond on heat-sensitive substrates (at ambient conditions).

Post-PLA, solute incorporation above a critical concentration makes the regrown solid solution unstable and causes the S/L interface to break apart into cellular structures. Assuming an isotropic solid–liquid interface during melt regrowth, the limiting concentration (C_s^{min}) of solute (sp^3-hybridized carbon) in the melt overlayer varies as

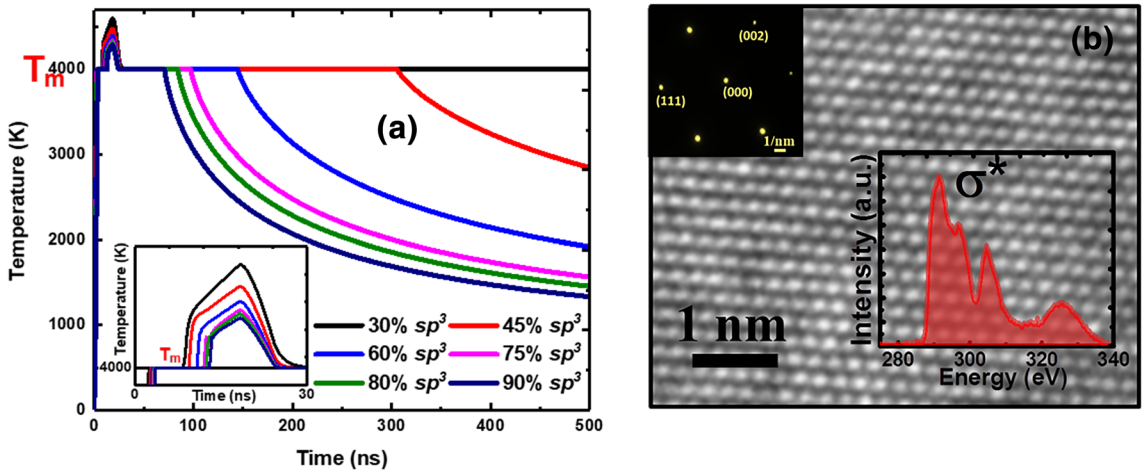

Fig. 4. (a) SLIM PLA thermal profiles for DLC/sapphire. The inset shows magnified profiles at the onset of melting for carbon and (b) HRTEM of ⟨110⟩ cross-section of diamond (homogeneous nucleation) with the insets showing the selected area diffraction pattern (⟨110⟩ single-crystal diamond) and core-loss EEL spectrum of diamond (indicating the presence of σ^* electronic states and a complete absence of π^* electronic states).

$$C_s^{\min} \propto \frac{Dk}{V(k-1)}\left(1+\frac{2k}{\left(1+\left(\frac{2\omega D}{V}\right)^2\right)^{\frac{1}{2}}-1}\right), \quad (6)$$

where D is the solute diffusion coefficient in the melt, V is the regrowth velocity, ω is the collective perturbation frequency, and k is the interfacial distribution coefficient.[16] Here, the cell size is given by $\lambda_{\min} = 2\pi/\omega_{\min}$. In the ultrafast regrowth regime ($V > 1$ m s^{-1}), the linear approximation for the solution of Eq. 6 leads to $\left(\frac{4\pi D}{\lambda V}\right) = Z$, where Z = constant. So, upon increase in regrowth velocity, the wavelength of instability is expected to decrease. This phenomenon is consistently observed in the thin films grown with varied sp^3 content. The wavelength of instability changed from 11 μm for 16% sp^3 to 5 μm for 48% sp^3 and $\sim$ 2 μm for 80% sp^3 laser-annealed DLC thin films. Analyzing the cell wavelength provides an estimate for the solid regrowth velocities from the melt state post-PLA.

CONCLUSION

This article provides estimates for the extent of undercooling and regrowth velocities based on experimental and theoretical considerations. We grew DLC thin films with varying sp^3 content from 16% to 80%. This series allowed us to analyze the relevant morphological changes in the microstructure of laser-annealed thin films and their dependence on the sp^3 content. It was found that the sp^3 content had a direct correlation with the undercooling and regrowth velocity. Hence, substrates with low thermal conductivity should facilitate diamond growth, while to grow Q-carbon nanostructures, use of thermally insulating substrates such as sapphire is advised. Utilizing this framework, one can standardize the processing parameters to limit the regrowth velocity, and in turn, solute trapping for PLA-processed boron- and nitrogen-doped Q-carbon multilayered films, thereby fabricating nanostructures exhibiting novel properties.

FUNDING

Funding was provided by National Science Foundation (Grant Nos. DMR-1735695 and DMR-1560838).

REFERENCES

1. J. Narayan, V. Godbole, and C. White, *Science* 252, 416 (1991).
2. J. Narayan and A. Bhaumik, *J. Appl. Phys.* 118, 215303 (2015).
3. J. Narayan and A. Bhaumik, *Mater. Res. Lett.* 4, 118 (2016).
4. S. Gupta, R. Sachan, A. Bhaumik, and J. Narayan, Unpublished research (2017).
5. A. Bhaumik, R. Sachan, and J. Narayan, *J. Appl. Phys.* 122, 045301 (2017).
6. J. Narayan and A. Bhaumik, *Mater. Res. Lett.* 5, 242 (2016).
7. H. Kumomi, *Appl. Phys. Lett.* 83, 434 (2003).
8. K. Jackson, *Surface Modification and Alloying* (Berlin: Springer, 1983), pp. 51–79.
9. J. Narayan, *J. Appl. Phys.* 53, 8607 (1982).
10. F. Spaepen, D. Turnbull, J. Poate, and J. Mayer, *Laser Annealing of Semiconductors* (New York: Academic, 1982), pp. 15–42.
11. NIST, *Chemistry Webbook*. http://webbook.nist.gov/cgi/cbook.cgi?ID=C7440440&Mask=2.
12. A. Cullis, N. Chew, H. Webber, and D.J. Smith, *J. Cryst. Growth* 68, 624 (1984).
13. R.K. Singh and J. Narayan, *Mater. Sci. Eng. B* 3, 217 (1989).
14. M. Shamsa, W. Liu, A. Balandin, C. Casiraghi, W. Milne, and A. Ferrari, *Appl. Phys. Lett.* 89, 161921 (2006).
15. B. Larson, J. Tischler, and D. Mills, *J. Mater. Res.* 1, 144 (1986).
16. J. Narayan, H. Naramoto, and C. White, *J. Appl. Phys.* 53, 912 (1982).